

ANALYSIS OF LIQUID SPRAY WITH AND WITHOUT HOMOGENEOUS BACKGROUND TURBULENCE

Douglas W Carter

Department of Aerospace Engineering and Mechanics
University of Minnesota
110 Union St SE, Minneapolis, MN 55414
carte775@umn.edu

Filippo Coletti

Department of Aerospace Engineering and Mechanics
University of Minnesota
110 Union St SE, Minneapolis, MN 55414
fcoletti@umn.edu

ABSTRACT

We employ a large chamber of homogeneous turbulence in a recently introduced facility to experimentally investigate the properties of a liquid water spray produced by a hollow-cone nozzle. We characterize the properties of the spray issued in quiescent and turbulent air, and in particular: the spray penetration, its mixing with the surrounding air, the droplet size distribution, and the related Eulerian and Lagrangian two-point correlations. This is the first study in which spray dynamics are investigated over the full range of relevant scales with and without a turbulent background. To this end we perform planar imaging at various spatial and temporal resolutions. Focusing on a window in the far field, we perform particle tracking velocimetry using a high-speed laser and camera system, and droplet sizing by shadowgraphy using a low-speed high-resolution camera mounted on a long-range microscope and synchronized with a pulsed LED. The resulting spray penetration and flow characteristics for cases with and without background turbulence are discussed.

INTRODUCTION

The efficient combustion of liquid fuel spray is of paramount importance for the performance of numerous energy systems, including the combustion of gas turbine engines. Therefore, understanding the processes of formation and dispersion of the droplets is critical to design the next generation of spray combustion systems. Optimizing these processes is however difficult because of the complexity and interactions among the several involved mechanisms, and several strategies have been pursued including: advanced atomizer geometry, acoustic and ultrasonic vibrations applied to the nozzles, piezoelectric actuators, and injection of gas bubbles. Here we focus on one aspect which is widely acknowledged to be crucial to determine the spray droplet properties and behavior, yet is not well understood: the interaction between the spray droplets and the gas turbulence.

APPARATUS AND METHODOLOGY

The apparatus used to generate controlled zero-mean homogeneous turbulence was qualified in the work of Carter *et al.* (2016), the turbulence characteristics of which were quantified in detail by Carter & Coletti (2017, 2018). The 5 m^3 acrylic chamber contains two facing panels which accommodate arrays of 128 ports each, fed by pressurized air at 700 kPa and controlled by solenoid valves. The latter are individually actuated by a National Instrument compact reconfigurable input/output system comprised of eight 32-channel output modules embedded in a 667MHz dual core controller, allowing for precise control of each individual valve. The valve outlets are connected with 1 mm brass nozzles screw-mounted at their end, producing choked jets of small mass flux, which entrain a much larger flow rate from the surroundings. Such an arrangement limits the formation of unwanted recirculating motions similarly to the random jet-stirred facility of Bellani & Variano (2014). The facility produces a homogeneous turbulent region with a volume of approximately $0.5 \times 0.7 \times 0.4\text{ m}^3$ at the center of the chamber. A conceptual sketch of the arrangement is shown in figure 1a.

Forcing and Spray Selection

The turbulence forcing is selected (see Carter *et al.*, 2016) to reflect typical values found in an engine combustor, the properties of which are displayed in table 1. These values reflect the properties of the air turbulence in the background, which are subsequently altered by the presence of the spray. The spraying system was chosen to be simple and well characterized, but also engine-relevant. We have used a hollow cone nozzle from Lechler Inc. (St. Charles, IL) Series 214, with a 1.8 mm orifice as shown in figure 1b. This was connected to a water supply and mounted at the bottom center of the turbulence chamber, directed vertically upward. Water at 25°C was provided by a vane pump (Procon Series 3, with a 0.5 HP Marathon Electric AC Motor). The pump was run at 5 bar yielding a flow rate of 470 mL/min as measured by an Omega Micro-Flo flow meter.



Figure 1. Conceptual cartoon (a) of experimental setup illustrating the turbulence chamber with centered upward-facing spray. A close-up picture of the Lechler Inc. Series 214 nozzle used to produce the liquid spray is shown in (b). The fields of view for the various measurements performed in the far-field of the spray are shown in (c), where the vertical dashed line is the spray axis, the red box the large-scale measurement region, the purple box the intermediate-scale region, and the green box the small-scale region. The inset of panel (c) corresponds to the dotted box.

Imaging Methods

We first perform large scale imaging to gain insight into features of the spray and obtain particle-image velocimetry measurements (PIV) of the collective droplet field with and without background turbulence. We used a Nd:YLF high-speed laser (Photonics Inc., 30 mJ/pulse) operated at 700 Hz, collimated by spherical and cylindrical lenses to form a 2 mm thick sheet. Imaging was performed with a 4 megapixel CMOS camera (Veo 640, Vision Research Inc.) mounting a 50 mm Nikon lens, allowing us to image a large-scale region 37 cm by 57 cm in size in the far-field of the spray as displayed in the red region in figure 1c. At this size, PIV final interrogation windows of 64 x 64 pixels correspond to 1.4 cm x 1.4 cm. With 50% overlap, the final vector spacing for the large-scale imaging is 0.7 cm x 0.7 cm.

Additional measurements at an intermediate scale were performed using a 200mm Nikon lens yielding a window 13 cm x 8 cm in size and data was instead collected at a frequency of 1200 Hz. The improved spatial and temporal resolution made possible identification of individual droplets for which particle tracking velocimetry (PTV) was employed. The intermediate scale data allows for quantification of droplet velocities as well as concentration, however cannot resolve the droplet sizes. The bottom of this window was located 600 mm (or 334 nozzle diameters) above the nozzle as displayed in the purple region of 1c.

In addition to high-speed imaging we perform low-speed high-resolution shadowgraphy utilizing a long-range microscope (Infinity K2 610088) mounted on a 29 megapixel CCD camera facing a pulsed LED light source (Hardsoft IL-105g) at a measurement location 380 diameters above the nozzle. The measurements allow to directly measure by backlighting the droplet sizes on a window 4.5 cm x 3.1 cm in size, yielding a resolution of approximately 7 μm per pixel. A sub-window is cropped to isolate the region of the shadowgraphs with the highest contrast, yielding a field of view 1.2 cm x 1.0 cm as shown in the green region of 1c. The droplet size distribution and mean diameter were found to well approximate the distribution measured by Lechler Inc using phase-doppler anemometry at the same operating conditions, confirming the robustness of the method. The thin depth of focus (≈ 3 mm) provided by the long-range microscope allows for accurate 2D evalua-

tion of the droplet distributions.

Table 1. Selected background turbulence properties in the chamber for settings ‘‘G5’’ and ‘‘B5’’: RMS velocity u_{rms} , integral length scale L , integral time scale T_L , dissipation rate of turbulent kinetic energy ε , Kolmogorov microscale η , Kolmogorov time scale τ_η , and the Taylor-microscale Reynolds number $Re_\lambda = u_{rms}\lambda/\nu$.

	G5	B5
u_{rms} [m/s]	0.34	0.61
L [cm]	12.3	15.8
T_L [s]	0.4	0.3
ε [m^2/s^3]	0.12	0.8
η [mm]	0.42	0.26
τ_η [ms]	3.6	4.5
Re_λ	255	412

Image Based Velocimetry

For all resolutions, data is obtained for spray issued into a quiescent and a turbulent background. For the large-scale time-resolved and small-scale time-independent data sets, the spray is issued into the ‘‘B5’’ turbulent background. For the intermediate-scale time-resolved data, the spray is issued into the ‘‘G5’’ turbulent background, see table 1.

The large-scale time-resolved data taken on the 37 cm x 57 cm window was processed using the Robust Phase-Correlation (RPC) method presented in Eckstein & Vlachos (2009) where the correlations peaks are improved by incorporating information related to various sources of potential PIV errors and performing correlations in phase space. In addition a multi-frame pyramid correlation algorithm (Sciaccitano *et al.* 2012) of order 3 is used to optimize the particle displacements using the temporal information. Accu-

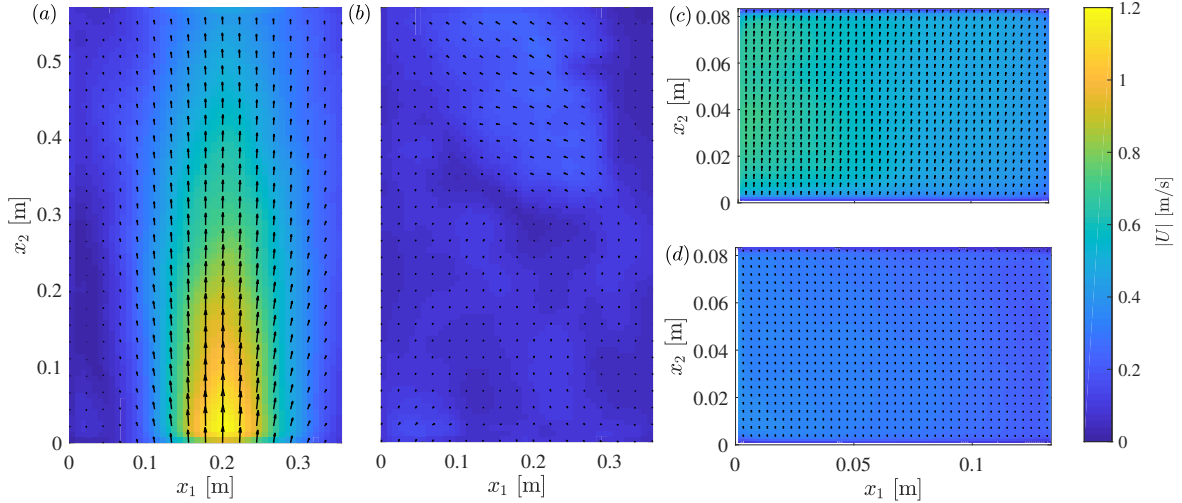


Figure 2. Large-scale (a,b) and intermediate-scale (c,d) mean velocity vectors of the droplets $U_i(x_1, x_2)$ for the quiescent background (a,c), the B5 turbulent background (b) and the G5 turbulent background (d). The mean field for the intermediate scale data is obtained through interpolation of the ungridded velocities onto a Cartesian grid at each instant.

accuracy is improved by first applying a mean background subtraction to the large-scale images. Standard outlier detection using median thresholding are applied to the PIV fields and flagged vectors are replaced using a standard bilinear interpolation. This resulted in replacing approximately 10% and 30% of vectors for the quiescent and turbulent background, respectively. For the quiescent background, 2000 time-resolved images are acquired in 5 separate runs. For the turbulent background, 1000 time-resolved images are acquired in 10 separate runs. This was done in order to help improve the statistics for the turbulent background, which is naturally slower to converge. Convergence tests on the spatial average of the mean droplet velocity fields indicate the value of the mean is converged to within 3% and 20% for the quiescent and turbulent background, respectively. Such convergence limits the analysis of the large-scale measurements to the most basic statistics.

The intermediate-scale time-resolved measurements taken on the 13 cm m x 8 cm window were analyzed using Particle Tracking Velocimetry (PTV) using the four-frame best estimate algorithm outlined in Ouellette, Xu & Bodenschatz (2006) to track their locations. The droplet positions were then convolved with a Gaussian kernel function to obtain smoothed velocities along each trajectory. To improve accuracy, the images were first background subtracted. For both the quiescent and the turbulent cases, five time-resolved data sets were collected at 1.2 kHz yielding 6200 images per data set. Although the number may fluctuate depending on the instant considered, $O(10^4)$ drops were identified in each image resulting in a total of $O(10^7)$ ungridded data points for both the quiescent and turbulent backgrounds. This resulted in satisfactory convergence of the mean fields to within a percent for both the quiescent and turbulent backgrounds and allows for investigation of in-depth statistics.

RESULTS

Spray Penetration

The penetration of the spray, quantified by the spatial mean flow distribution ($U_i = u_i - u'_i$ where u_i , U_i , and u'_i

are the raw, mean, and fluctuating in-plane velocity components, respectively) was found to be attenuated in the presence of background turbulence. This is shown for the B5 turbulent background using the large-scale PIV measurements as well as the G5 turbulent background from the intermediate scale PTV measurements in figure 2. The large-scale velocity fields reveal that the intense B5 background turbulence prevents any recognizable spray plume from reaching the field of view. On the other hand the intermediate-scale measurements with G5 background turbulence, which is weaker compared to the B5, does have a clear mean upward velocity indicating the some of the spray momentum reaches the field of view, although it's mean magnitude is significantly reduced.

Droplet Trajectories

Extensive droplet statistics were obtained for the Lagrangian trajectories of the PTV data taken on the intermediate-scale resolution. From these the relevant spatial and temporal time scales as well as concentration field statistics are obtained and presented in the following.

Velocities The spatial and temporal properties of the spray velocities are quantitatively understood via the two-point autocorrelations. In space, this is performed using the Eulerian autocorrelation

$$\rho_{u_i}(r) = \frac{\langle u'_i(x)u'_i(x+r) \rangle}{\langle u'_i(x)^2 \rangle} \quad (1)$$

where $\langle \dots \rangle$ denotes statistical ensemble averaging, x corresponds to position and r the separation distance. In time the particle tracks may be used to investigate the Lagrangian autocorrelation

$$\rho_{u_i}(\tau) = \frac{\langle u'_i(t)u'_i(t+\tau) \rangle}{\langle u'_i(t)^2 \rangle} \quad (2)$$

where t is the time and τ the temporal lag. The dependence of ρ_{u_i} on x and t is dropped under the approximation of spatial homogeneity in x and temporal steadiness in t . This

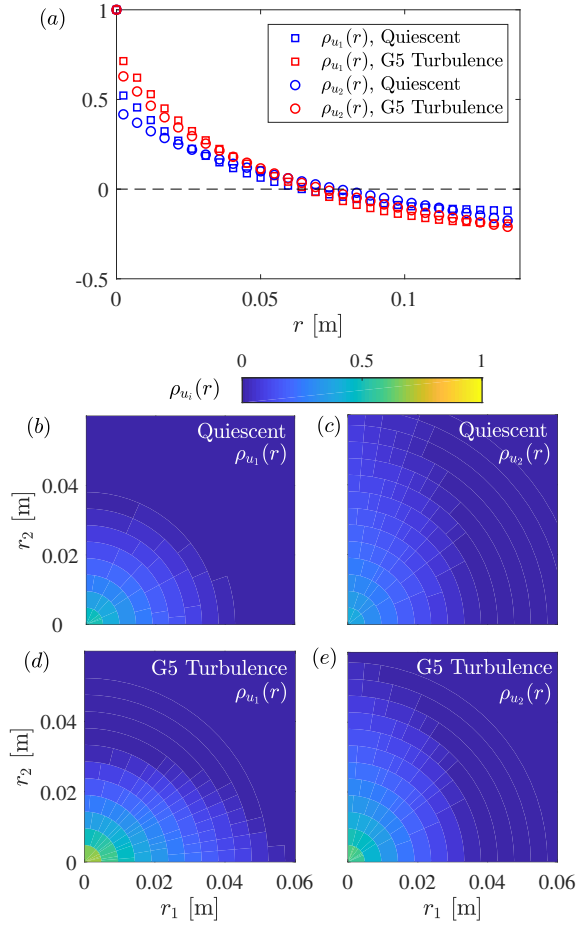


Figure 3. Orientation-averaged Eulerian autocorrelations $\rho_{u_i}(r)$ for quiescent (blue) and G5 turbulence (red) backgrounds for u_1 (squares) and u_2 (circles) (a) and the same functions before averaging over orientations in r -space (b,c,d,e).

was tested for by calculating autocorrelations at various x and t , for which the variation was found to be small.

The spatial Eulerian autocorrelations $\rho_{u_i}(r)$ are presented in figure 3. In figure 3a the orientation-averaged autocorrelations show a clear drop in magnitude at near zero separation. This drop could be due to noise in the PTV measurements, however the Gaussian smoothing kernel applied to the trajectories mitigates the effect of measurement noise on the autocorrelations. This smoothing was shown to reduce the drop of $\rho_{u_i}(r)$ as $r \rightarrow 0$, but only by a few percent. For particles in turbulence, such a drop in the spatial autocorrelation as $r \rightarrow 0$ is a known affect attributed to random uncorrelated motion caused by the particles own excess inertia with respect to the inertia of the fluid (Vance *et al.*, 2006). In the presence of a turbulent background, the inertia of the air is effectively enhanced; reducing the effect of random uncorrelated motion. As a result, the Eulerian autocorrelations do not drop as significantly in the presence of a turbulent background for both u_1 and u_2 components.

The Eulerian autocorrelations in all of (r_1, r_2) , binned into 20 solid angles between 0 and $\pi/2$, are shown in figure 3b-e. In homogeneous and isotropic turbulence the fluctuating velocity fields have Eulerian autocorrelations in r -space with an aspect ratio equal to two, flipped ninety degrees

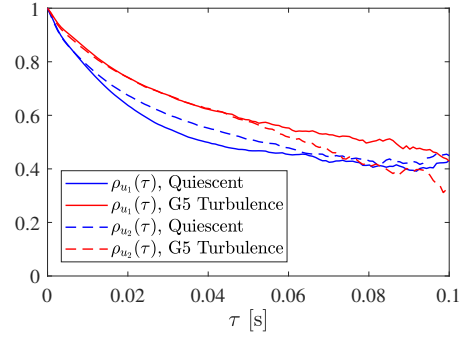


Figure 4. Lagrangian autocorrelation $\rho_{u_i}(\tau)$ for quiescent (blue) and G5 (red) turbulence backgrounds for u_1 (solid) and u_2 (dashed).

with respect to one another for u_1 and u_2 . Such a trend appears to be at least qualitatively consistent for the Eulerian autocorrelations of the droplets presented here, with some notable differences. Besides the drop in ρ_{u_i} as $r \rightarrow 0$, the correlations quickly plunge into negative values. This is likely due to the crossing trajectory effect (Squires & Eaton 1991).

The Lagrangian autocorrelations $\rho_{u_i}(\tau)$ of the droplet velocities are presented in figure 4. As the lag time τ increases, the number of trajectories having length τ diminishes quickly, as is reflected by the jitter in the trend lines for higher and higher values of τ . The droplets in the quiescent background decorrelate in time more quickly than those in the turbulent background. This indicates that the larger integral time scales of the homogeneous turbulence background are felt by the droplets and reflected in their Lagrangian autocorrelation. In the quiescent background, the vertical velocity correlates over slightly longer times τ , however this difference is not seen in the turbulence background. This is likely due to the turbulent mixing, causing the time scales over which each velocity is correlated to approach each other.

Concentration The concentration fields are obtained at each instant using the Voronoi method described in Monchaux *et al.* (2010), where a cell is defined around each droplet at each instant using the midpoints between each droplet and all surrounding droplets. A sample voronoi diagram is shown for the quiescent case in figure 5a. As can be seen, the area of each cell A is inversely proportional to the local concentration of droplets. By comparing the probability density function of interior cell areas to that of a Random Poisson Process (RPP, represented in 2D using a Gamma function as described in Ferenc & Néda 2007), which describes the distribution all cell areas for a random set of points, the local concentration can be intrinsically quantified. Figure 5b shows that both the quiescent and turbulent background have a degree of preferential concentration of the droplets, with the droplets in the turbulent background exhibiting stronger clustering.

Similarly to the velocity fluctuations, the local concentration c can be decomposed into a mean $\langle c \rangle$ and fluctuating part c' such that $\langle c \rangle = c - c'$. Using the inverse Voronoi area A^{-1} as a proxy for concentration such that $c' = A^{-1} - \langle A^{-1} \rangle$, the Eulerian and Lagrangian autocorrelations of concentration are defined as

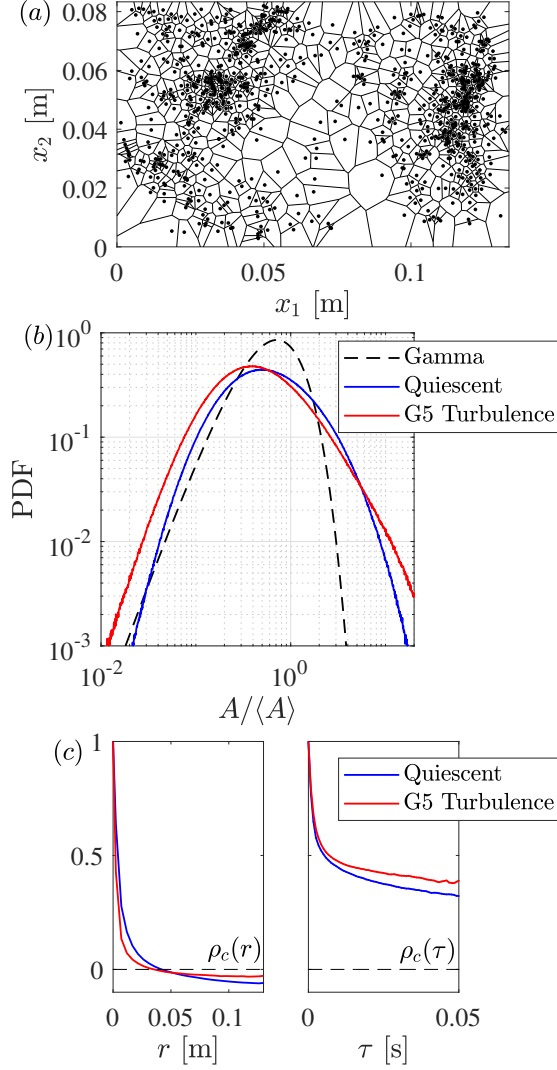


Figure 5. Voronoi diagram generated for an instantaneous sample of the droplet field with a quiescent background (a) and Voronoi PDFs over all samples for the quiescent background (blue) and turbulent background (red) with a 2D gamma distribution for comparison (dashed) (b). The Eulerian and Lagrangian autocorrelations of the concentration using the inverse Voronoi areas are displayed in (c).

$$\rho_c(r) = \frac{\langle c'(x)c'(x+r) \rangle}{\langle c'(x)^2 \rangle} \quad (3)$$

and

$$\rho_c(\tau) = \frac{\langle c'(t)c'(t+\tau) \rangle}{\langle c'(t)^2 \rangle} \quad (4)$$

respectively. The autocorrelations of the concentration fields ρ_c are displayed in figure 5c for both quiescent and G5 turbulence backgrounds. These include all interior points and are not limited to droplets which are within clusters or voids. The Eulerian autocorrelations of concentration $\rho_c(r)$ rapidly decorrelate in space, indicating limited spatial coherence. This occurs more quickly for the droplets in a turbulent background. On the other hand, the Lagrangian autocorrelations of concentration, although they also initially drop quickly, remain partially correlated for appreciable

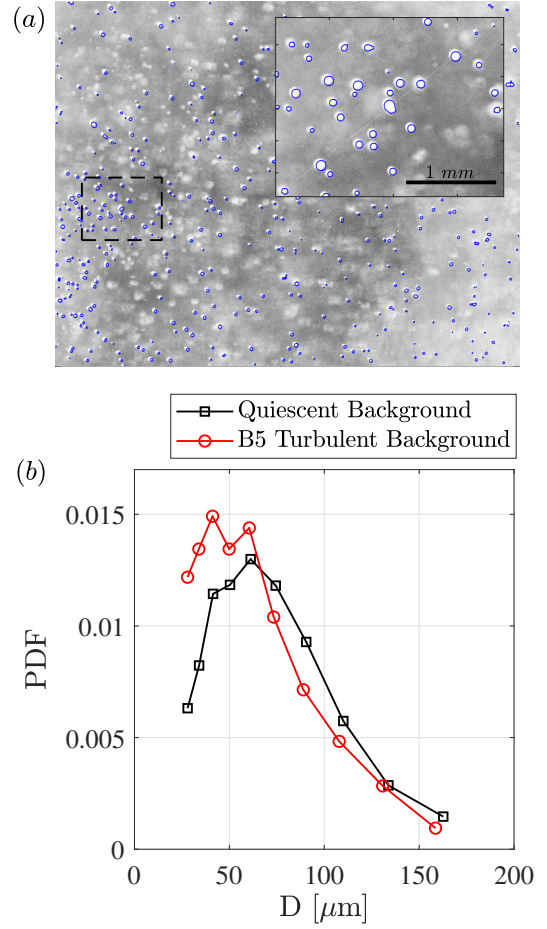


Figure 6. Inverted shadowgraph for an instantaneous sample of droplets in a quiescent background (a), with inset corresponding to the dashed boxed region. The blue contours correspond to the sizing threshold. The PDF of droplet size distributions for the quiescent (black squares) and B5 turbulence (red circles) background are shown in (b).

separation times τ . In this case, the turbulence background has a higher droplet autocorrelation. The exact cause of this behavior is unclear, but points to a temporal persistence of concentration along the droplet trajectories.

Droplet Size Distributions

The droplet size distributions obtained using high-resolution small-scale shadowgraphy are presented in figure 6. Figure 6a displays a sample shadowgraph for the droplets issued into a quiescent background. A threshold was manually determined in order to distinguish droplets from the background, which may contain noise as well as out of focus droplets. To improve accuracy, a minimum area threshold of 9 pixels was imposed as well as an aspect ratio threshold of detected objects whose aspect ratio was found to be less than 1.5. This limited the detection of droplets which were under-resolved and/or overlapping, respectively. As such the minimum detectable equivalent diameter is approximately 14 μm . According to phase doppler anemometry measurements of the same spray at the same operating conditions as provided by the manufacturer, droplets of this size comprise less than approximately 10%

of all droplets.

The resulting PDFs of the droplet size distributions using the equivalent diameter $D = \sqrt{\frac{4}{\pi} A_{drop}}$ in figure 6b show similar trends between the two cases, with the droplet size distribution in the turbulent background shifted slightly to the left. The mean equivalent diameter (D) was found to be $64 \mu\text{m}$ and $57 \mu\text{m}$ for the quiescent and turbulent backgrounds, respectively. This points to the possibility of droplet breakup occurring in the presence of the turbulent background. It should be noted however that a pixel resolution of $7 \mu\text{m}$ limits the certainty of this conclusion.

DISCUSSION

The characteristics of spray issued into a quiescent and homogeneous turbulence background have been presented at multiple resolutions. The large-scale time-resolved measurements revealed that the inertia of the spray was itself insufficient to penetrate into the homogeneous turbulent region for the B5 turbulence forcing. Intermediate-scale resolution measurements however reveal that the upward momentum of the spray was still retained for the weak G5 turbulence forcing, with a reduced vertical mean velocity magnitude of approximately 30% the quiescent magnitude.

The droplet trajectories obtained from the intermediate-scale measurements revealed interesting dynamics through use of the Eulerian and Lagrangian autocorrelation functions of velocity and concentration. The turbulence background generally increased the length and time scales over which the velocity components correlated, indicating that the droplets were influenced by the presence of energetic large-scale eddies. The inertial droplets showed an initial drop in the Eulerian autocorrelations of velocity indicative of the presence of random uncorrelated motion. The effect of random uncorrelated motion was found to be reduced in the presence of a turbulence background, supporting the notion that the effective inertia of the droplet (with respect to the time scale of the air) is augmented by the background turbulence. Using a Voronoi analysis, it was shown that the spray issued into quiescent air itself displayed preferential concentration phenomena, the degree of which is enhanced when the background air is turbulent. Autocorrelations of the concentration field reveal that the droplets quickly decorrelate spatially, however remain partially correlated temporally. This mechanism through which this occurs is unclear and requires further examination.

The droplet size distributions obtained using high-resolution shadowgraphy revealed good agreement with independent measurements of the same spray at the same

operating conditions, however the decrease in the droplet sizes in the presence of a turbulent background were only marginally conclusive due to the limited resolution.

Acknowledgements

The authors gratefully acknowledge support from the Office of Naval Research (grant N00014-17-1-2578) as well as P. Vlachos and J. Eshraghi for their support on implementing the RPC PIV code.

REFERENCES

- Bellani, Gabriele & Variano, Evan A 2014 Homogeneity and isotropy in a laboratory turbulent flow. *Experiments in fluids* **55** (1), 1646.
- Carter, Douglas, Petersen, Alec, Amili, Omid & Coletti, Filippo 2016 Generating and controlling homogeneous air turbulence using random jet arrays. *Experiments in Fluids* **57** (12), 189.
- Carter, Douglas W & Coletti, Filippo 2017 Scale-to-scale anisotropy in homogeneous turbulence. *Journal of Fluid Mechanics* **827**, 250–284.
- Carter, Douglas W. & Coletti, Filippo 2018 Small-scale structure and energy transfer in homogeneous turbulence. *Journal of Fluid Mechanics* **854**, 505543.
- Eckstein, Adric & Vlachos, Pavlos P 2009 Digital particle image velocimetry (dpiv) robust phase correlation. *Measurement Science and Technology* **20** (5), 055401.
- Ferenc, Járjai-Szabó & Néda, Zoltán 2007 On the size distribution of poisson voronoi cells. *Physica A: Statistical Mechanics and its Applications* **385** (2), 518–526.
- Monchaux, Romain, Bourgoïn, Mickaël & Cartellier, Alain 2010 Preferential concentration of heavy particles: a voronoi analysis. *Physics of Fluids* **22** (10), 103304.
- Ouellette, Nicholas T, Xu, Haitao & Bodenschatz, Eberhard 2006 A quantitative study of three-dimensional lagrangian particle tracking algorithms. *Experiments in Fluids* **40** (2), 301–313.
- Sciacchitano, Andrea, Scarano, Fulvio & Wieneke, Bernhard 2012 Multi-frame pyramid correlation for time-resolved piv. *Experiments in fluids* **53** (4), 1087–1105.
- Squires, Kyle D & Eaton, John K 1991 Measurements of particle dispersion obtained from direct numerical simulations of isotropic turbulence. *Journal of Fluid Mechanics* **226**, 1–35.
- Vance, Marion W, Squires, Kyle D & Simonin, Olivier 2006 Properties of the particle velocity field in gas-solid turbulent channel flow. *Physics of Fluids* **18** (6), 063302.